Volume 50
Number 3
21 January 2021
Pages 757-1128

Dalton Transactions

An international journal of inorganic chemistry

rsc.li/dalton

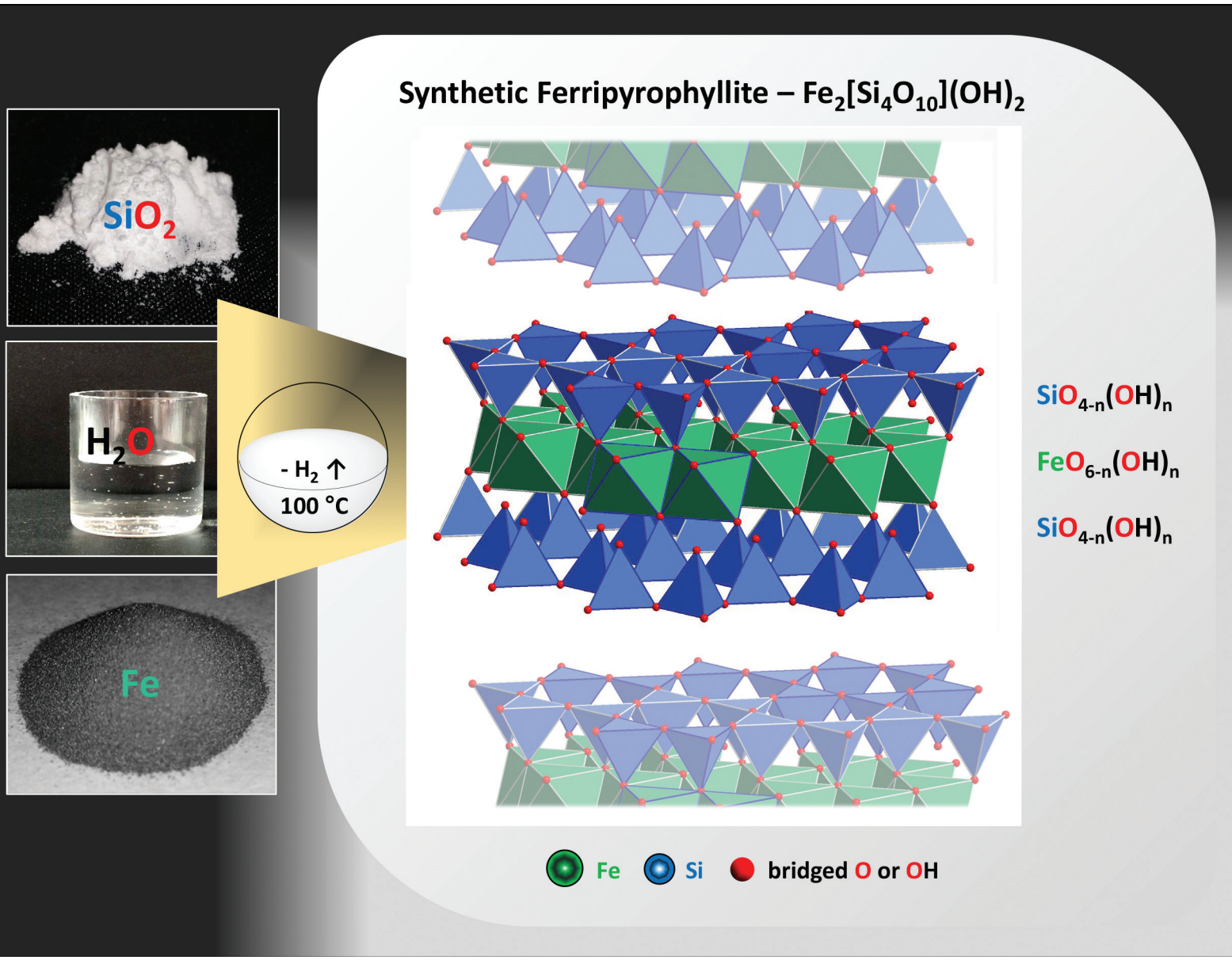

ISSN 1477-9226

ROYAL SOCIETY OF CHEMISTRY

PAPER
Nils Theyssen, Walter Leitner *et al.*
Synthetic ferripyrophyllite: preparation, characterization and catalytic application

50 Anniversary Volume

Dalton Transactions

ROYAL SOCIETY OF CHEMISTRY

PAPER

View Article Online
View Journal | View Issue

Cite this: *Dalton Trans.*, 2021, **50**, 850

Synthetic ferripyrophyllite: preparation, characterization and catalytic application†

Yunxiang Qiao, [a,b] Nils Theyssen, *[a] Bernd Spliethoff,[a] Jan Folke, [b] Claudia Weidenthaler, [a] Wolfgang Schmidt, [a] Gonzalo Prieto, [a,c] Cristina Ochoa-Hernández, [a] Eckhard Bill, [a,b] Shengfa Ye, [a,b,d] Holger Ruland, [b] Ferdi Schüth [a] and Walter Leitner *[b,e]

Received 7th September 2020,
Accepted 5th January 2021

DOI: 10.1039/d0dt03125a

rsc.li/dalton

Sheet silicates, also known as phyllosilicates, contain parallel sheets of tetrahedral silicate built up by $[Si_2O_5]^{2-}$ entities connected through intermediate metal–oxygen octahedral layers. The well-known minerals talc and pyrophyllite are belonging to this group based on magnesium and aluminium, respectively. Surprisingly, the ferric analogue rarely occurs in nature and is found in mixtures and conglomerates with other materials only. While partial incorporation of iron into pyrophyllites has been achieved, no synthetic protocol for purely iron-based pyrophyllite has been published yet. Here we report about the first artificial synthesis of ferripyrophyllite under exceptional mild conditions. A similar ultrathin two-dimensional (2D) nanosheet morphology is obtained as in talc or pyrophyllite but with iron(III) as a central metal. The high surface material exhibits a remarkably high thermostability. It shows some catalytic activity in ammonia synthesis and can serve as catalyst support material for noble metal nanoparticles.

Introduction

Phyllosilicates contain parallel sheets of tetrahedral silicate built up by $[Si_2O_5]^{2-}$ entities (Fig. 1).[1–3] They are an important group of minerals that includes the clay minerals as well as the groups of mica, chlorite, serpentine and talc/pyrophyllite.

Minerals of the latter group contain three layers: silicate tetrahedral layers are located on the top and on the bottom (indicated by $[Si_4O_{10}]$ in the formula), which are connected *via* a metal–oxygen octahedral layer. Materials with such tetrahedral/octrahedral/tetrahderal arrangements are classified as TOT sheet silicates.[4,5] Pyrophyllite is aluminum-based ($Al_2[Si_4O_{10}](OH)_2$) and talc is magnesium-based ($Mg_3[Si_4O_{10}](OH)_2$). The ferric analogue of pyrophyllite, known as ferripyrophyllite, has the idealized formula $Fe_2[Si_4O_{10}](OH)_2$ and was first reported by F.V. Chukhrov *et al.* in 1978.[6,7] It is found as a natural mineral only in mixtures or conglomerates with lots of impurities. The structure of ferripyrophyllite is shown in Fig. 2.[1,5,8,9] It is a dioctahedral TOT sheet silicate in which two-thirds of the octahedra are occupied with iron(III) centers, with hydroxyl groups attached.

Although the hydrothermal formation of transition metal phyllosilicates is known for cobalt,[11] nickel,[12] cobalt–nickel mixtures[13] and copper,[14] no synthetic protocol for iron-based pyrophyllite has been reported to the best of our knowledge yet.[10] Prominent iron silicate minerals are fayalite (Fe_2SiO_4),[15] ferrosilite ($FeSiO_3$ or $Fe_2Si_2O_6$),[16–18] iscorite ($Fe(II)_5Fe(III)_2SiO_{10}$)[19,20] and greenalite ($[Fe(II), Fe(III)]_{2\text{-}3}\ Si_2O_5(OH)_4$).[21,22] They are either formed under rather severe reaction conditions (>1000 °C, high pressure) or only found in nature.

Herein, we describe the discovery of Ferripyrophyllite formation at mild temperatures and almost ambient pressure.

[a]*Max-Planck-Institut für Kohlenforschung, Kaiser-Wilhelm-Platz 1, 45470 Mülheim an der Ruhr, Germany. E-mail: theyssen@kofo.mpg.de*
[b]*Max Planck Institute for Chemical Energy Conversion, Stiftstr. 34-36, 45470 Mülheim an der Ruhr, Germany. E-mail: walter.leitner@cec.mpg.de*
[c]*ITQ Instituto de Tecnología Química, Universitat Politècnica de València-Consejo Superior de Investigaciones Científicas (UPV-CSIC), Avenida de los Naranjos s/n, 46022 Valencia, Spain*
[d]*Dalian Institute of Chemical Physics, Chinese Academy of Sciences, 457 Zhongshan Road, 116023 Dalian, PR China*
[e]*Institut für Technische und Makromolekulare Chemie, RWTH Aachen University, Worringerweg 1, 52074 Aachen, Germany*

†Electronic supplementary information (ESI) available. See DOI: 10.1039/d0dt03125a

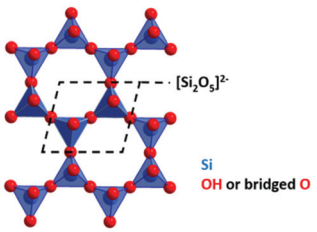

Fig. 1 $[Si_2O_5]^{2-}$ as basic structure units of sheet silicates (top view).

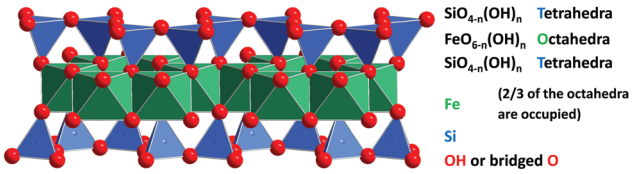

Fig. 2 Two unit cells of Ferripyrophyllite – the proposed structure of the iron silicate described herein (side view).

The initial isolation resulted from serendipitous observations carrying out catalytic reactions with SBA-15 material in aqueous media in steel reactors. Based on this initial finding, a reproducible synthetic protocol was developed that allows the usage of different silica sources (including for example also MCM-41, AlSBA-15, and aerosil) in combination with simple Fe powder in water. The preparation is typically performed at 100 °C in sealed stainless steel autoclaves (with glass inlet) under initial ambient pressure of air (see ESI for experimental details and S1–S11 for TEM and EDX analyses†).

Results and discussion

Material characterization

The standard synthetic method produces a beige homogeneous Fe-silicate material that is typically contaminated with small amounts of SiO_2. The morphology is best described as a continuous two-dimensional (2D) nanosheet structure (Fig. 3), resulting in a relatively large BET surface area of 273 $m^2\ g^{-1}$ and a total pore volume of 0.568 $cm^3\ g^{-1}$. Its CO_2 sorption capacity at 273 K was measured to be 5 $cm^3\ g^{-1}$ at 100 mbar and 20 $cm^3\ g^{-1}$ at 1000 mbar (Fig. S13†).[23]

According to TEM analysis, the apparent thickness of the nanosheets were in a range between 0.5 and 0.8 nm, which is consistent with the theoretical value of 0.7 nm (Fig. S12†). While parallel formation of a thinner TO sheet silicate cannot be ruled out completely, we have no evidence from any of our analytical techniques.

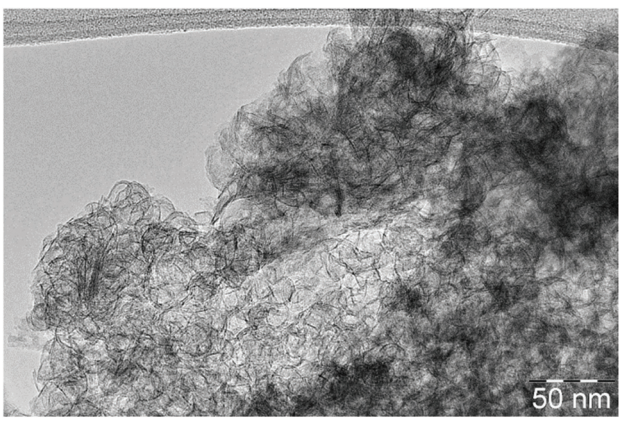

Fig. 3 TEM image of iron silicate nanosheets synthesized from iron powder and SBA-15 at 100 °C in water.

The oxidation of metallic iron to Fe(III) centers during the synthesis is accompanied by proton reduction according to eqn (1). The evolution of hydrogen is indicated by a distinct pressure increase during the reaction and was confirmed *via* GC analysis of the gas phase. The presence of about 4.89 mmol g^{-1} hydroxyl groups in the iron silicate (8.31 wt%, after drying at 100 °C for 12 h to remove physisorbed water) as determined by titration[24,25] also accounts for the OH^- formation.

$$2\ Fe^0 + 6\ H_2O \rightarrow 2\ Fe^{3+} + 6\ OH^- + 3\ H_2 \quad (1)$$

X-ray photoelectron spectroscopy (XPS) revealed an atomic ratio of Fe to Si of exactly 1 : 2 on the surface of the material. The XPS spectrum of Si 2p shows a single peak at 103.1 eV (Fig. S14†), which is well within the reported values for silicates (101.6–103.8 eV).[26,27] The spectra of Fe 2p1/2 and Fe 2p3/2 show characteristic peaks at 725.6 and 712.0 eV, together with associated satellite peaks (Fig. S15†). Combined with the single peak of Fe 3p at 56.9 eV, a clear dominance of Fe(III) centers can be deduced from these data.[28,29]

The Fe(III) oxidation state is further confirmed by ^{57}Fe Mössbauer spectroscopy (Fig. S16†).[30–34] The small isomer shift of about 0.36 mms^{-1} at room temperature indicates Fe(III) high spin centers with six hard ligands, which are expected to be oxygen. A defined coordination environment is difficult to deduce, however, because the quadrupole splitting is quite large (about 0.79 mm s^{-1}), showing deviations from cubic symmetry. Furthermore, the high experimental line width of about 0.74 mm s^{-1}, which could be fitted with a Gaussian distribution of Lorentzian lines, points to heterogeneities and an overlap of several similar lattice sites. Almost 100% Fe(III) species were found to be present, a minor subspectrum (max. 7%) indicates the presence of only traces of Fe(II) species. A broad peak in the EPR spectrum (Fig. S17†) is typical of ferromagnetic resonances of small magnetic domains.[35] Magnetization curves under zero-field-cooled (ZFC) and field-cooled (FC) conditions confirm that this iron silicate is paramagnetic or superparamagnetic (Fig. S18†).

Composition analysis with a combination of Energy-Dispersive X-ray spectroscopy (EDX) and Scanning Transmission Electron Microscopy (STEM) revealed a very uniform distribution of the elements Fe, Si and O in the nanosheets (Fig. 4), measuring an average composition of $FeSi_{2.0}O_{8.0}$ for the specific sample. EDX bulk analysis of iron silicates from five different batches gave an average composition of $FeSi_{2.0}O_{6.4}$. Another 76 EDX-analyses in combination with high resolution TEM allowed sampling directly at the nanosheet structures. These measurements resulted in an average composition of $FeSi_{1.7\pm0.2}\ O_{5.2\pm0.4}$ (confidence level P = 95%).

The silicon-to-iron ratio of 2 : 1, together with clearly dominating Fe(III) centers are consistent with double chain silicates of the amphibole subgroup such as $Fe_2[Si_4O_{11}]$ as well as with sheet silicates of the serpentine subgroup of phyllosilicates such as $Fe_2[Si_4O_{10}](OH)_2$.

The already mentioned content of hydroxyl groups (8.31 wt%) measured *via* titration fits well with the chemical

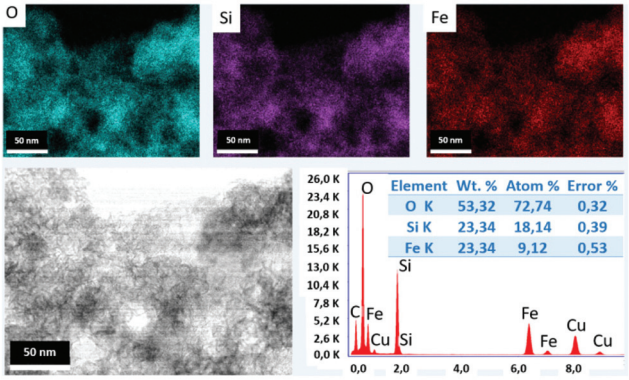

Fig. 4 STEM-EDX mapping of the synthetic iron silicate nanosheets.

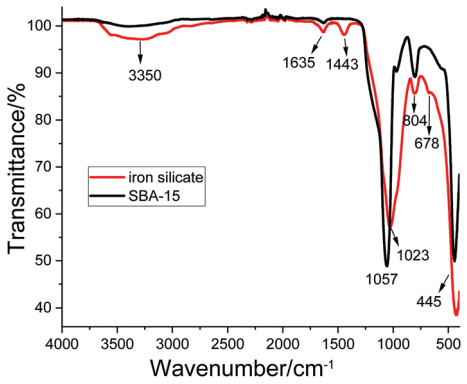

Fig. 6 ATR-IR spectra of SBA-15 and the obtained iron silicate after hydrothermal synthesis.

formula $Fe_2[Si_4O_{10}](OH)_2$, corresponding to 8.13 wt% hydroxyl groups theoretically. Further evidence for this composition results from the hydrogenative decomposition of the material in a temperature window between room temperature and 500 °C over 13 h. A total amount of 6.1 mmol water was formed from a sample of 1.458 mmol iron silicate as measured *via* integration of a calibrated online IR-detector signal (Fig. S19†), matching the stoichiometry for a sheet silicate in eqn (3) more closely than for eqn (2).

$$Fe_2[Si_4O_{11}] + 3H_2 \rightarrow 2\ Fe + 4\ SiO_2 + 3H_2O \quad (2)$$

$$Fe_2[Si_4O_{10}](OH)_2 + 3H_2 \rightarrow 2\ Fe + 4SiO_2 + 4H_2O \quad (3)$$

The absence of characteristic features of $FeSiO_4$ and Fe_2O_3 in pair distribution function (PDF) analysis further confirms a unique structure rather than a mixture of these two known materials (Fig. S20†).[36,37] Comparing the main atom distances as derived from the peak maxima in the iron silicate with other known materials indicates a coordination of iron with bridged oxygen atoms and hydroxyl groups (labelled as FeO(OH)). Such entities are in fact also present in Ferripyrophylite (Fig. 2), and the measured data correlates nicely with simulated data of this structure (Fig. 5).

The existence of Fe–O–Si units in the material was evidenced by ATR-IR spectroscopy.[38–43] While physical mixtures of Fe_2O_3 and SBA-15 showed only the additive signals of the two components (Fig. S21†), distinct differences are evident for the new material (Fig. 6 and also Fig. S22†). The characteristic absorbance of silica at 1057 cm^{-1} (asymmetric Si–O–Si stretching) was shifted to the lower frequency at 1023 cm^{-1}, with concomitant inversion of the transmission ratio to the absorbance at 445 cm^{-1} (O–Si–O bending). Together with the shoulder at 678 cm^{-1} (Si–O–Fe symmetric stretching mode), this provides strong evidence for the extensive incorporation of iron atoms in the silica framework. The absorbance at 1443 cm^{-1} can be assigned to FeOOH units,[44,45] correlating with its presence from PDF analysis. The broad band around 3350 cm^{-1} and the peak at 1635 cm^{-1} are assigned to O–H stretching (involving hydrogen bond interactions) and bending modes of adsorbed water, respectively.[46]

Upon heating the material at 450 °C for 4 h under vacuum to initiate dehydration, the OH stretching vibration region showed a sharp band at 3745 cm^{-1} (in the absorbance mode only) ascribed to the presence of the terminal silanol groups (Si–OH) (Fig. S23a†) The acidity of this material was assessed by pyridine adsorption/desorption. After pyridine desorption at 150 °C (Fig. S23b†), the iron silicate exhibits two bands at 1610 and 1450 cm^{-1} associated with pyridine coordinated Lewis acid sites. Very weak bands at 1637 and 1545 cm^{-1} characteristic of pyridinium ions (PyH^+) indicate the presence of low amounts of Brønsted acid sites.[47,48] When desorption temperature increases up to 250 °C, the band intensities drop, indicating the presence of acid sites with different strengths.

A series of NH_3-TPD measurements have been performed in order to evaluate the surface acidity of the iron silicate material relative to standard silica–alumina solid acids (Fig. S24–S27†). The acid site density (per mass of the sample) and acid strength were found to be comparable with that of amorphous SiO_2–Al_2O_3 materials.

The iron(III) silicate is chemically quite stable in weak bases. In fact, it was purified from a 6 M NH_3 solution. However, it is not stable towards strong bases like diluted NaOH solutions. Moreover, it decomposes in acidic media, like diluted mineral acids such as HCl, H_2SO_4, and HF (1 M).

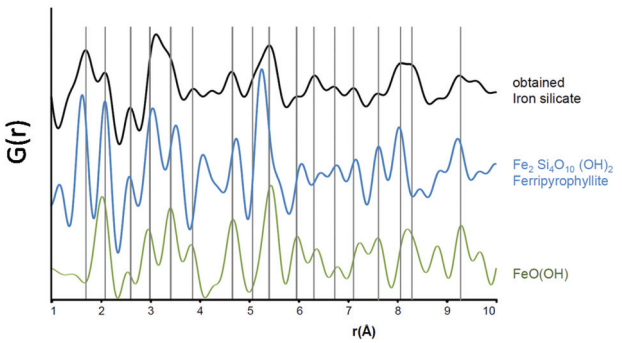

Fig. 5 Pair distribution function (PDF) analysis of the iron silicate compared to simulated PDFs for Ferripyrophylite and FeO(OH).

Thermostability of the iron silicate is very high, as evidenced by temperature-dependent X-ray diffraction (XRD) measurements (Fig. S28†). Only broad peaks were detected due to the thin sheet structutre. Interestingly, the pattern is not reported in any of the screened databases. Slight peak shifts were observed after calcination under synthetic air at 300 °C (Fig. S29†), consistent with reported dehydration temperatures of FeO(OH) units between 250 and 300 °C.[49–52] This interpretation is supported by *in situ* diffuse reflectance infrared Fourier transform spectroscopy (DRIFT) indicating concomitant disappearance of the absorbance at 1440 cm^{-1} (Fig. S30†). ^{57}Fe Mössbauer spectroscopy suggests the preservation of the Fe-silicate structure at this stage (Fig. S31 and S32†).

No further changes were observed in the XRD pattern upon heating up to 800 °C in synthetic air (Fig. S28†). The BET surface area remained high at about 182 $m^2\ g^{-1}$ (Fig. S33†). TEM investigations showed that the ultrathin iron silicate sheets remained intact even after three hours at 600 °C (Fig. 7). EDX analysis on seven different locations revealed an average composition of $FeSi_{2.0}O_{5.6}$ fully in line with the native material.

Only at temperatures around 1000 °C, the material converts to SiO_2 and Fe_2O_3 according to TEM and XRD analyses (Fig. S34 and S35†). Exchanging the oxidative atmosphere with pure nitrogen, temperature-dependent XRD measurements show phase transitions already between 550 and 600 °C. The new phases remain stable up to 850 °C and prevail also after cooling to room temperature (Fig. S36†). The new reflections could be assigned to Fayalite and Fe_3O_4 (Fig. S37†). Under inert atmosphere, the reduction is accompanied with oxygen evolution. TG-DSC-MS analysis under argon revealed the loss of molecular O_2 in addition to water. In contrast, only water was detected under air, explaining the higher temperature stability of the iron silicate under air as compared to inert atmospheres (Fig. S38 and S39†).

Ultrathin 2D-nanostructures are finding great attention due to a broad spectrum of interesting properties related to their chemical, electrochemical, catalytic, electronic, optical, magnetic or thermal characteristics.[53] A variety of applications has emerged, covering the areas of catalysis[54–56] as well as energy storage devices, sensors, gas storage materials and others.[57]

Due to the good thermal stability and high surface area, the iron silicate was used as a support material for Pd catalysts synthesized by chemical fluid reactive deposition.[58] The Pd-decorated material was tested for hydrogenation of unsaturated compounds, and high conversions and yields were obtained under standard screening conditions (Table 1). In comparison with 3 wt% Pd/SBA-15 and Pd/C under otherwise identical reaction conditions (not shown here), deoxyfunctionalization is much less pronounced. Instead, the formation of benzylic alcohols is preferred (entries 2–5). Interesting is also the relatively high selectivity for hydrogenation of the aromatic ring in entry 6, while the benzene ring of benzylidene acetone remained intact (entry 7). Furthermore, 3% Pd/iron silicate showed good stability and reusability in the hydrogenation of this substrate as shown in the ESI in Table S1.† The reduced conversion from run 5 onwards seems to be caused mainly by incomplete catalyst recovery rather than deactivation. So further studies in particular for hydrogenation of multifunctional compounds seem promising.[59,60]

Finally, the iron silicate was also tested as a catalyst precursor in ammonia synthesis (Fig. S40†).[61–66] The comparison of the activity with a model catalyst ($MgFe_2O_4$),[61] and a state-of-the-art industrial catalyst at different temperatures is shown in

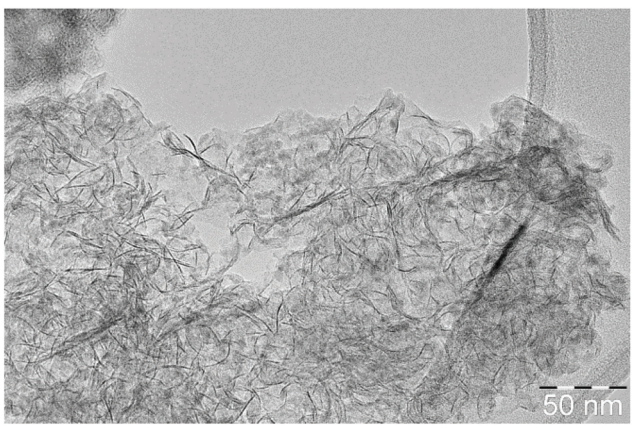

Fig. 7 TEM images of iron silicate after heating the sample to 600 °C for 3 h under synthetic air.

Table 1 Catalytic data of hydrogenation using 3 wt% Pd/iron silicate as catalyst

Entry	Substrate	Conv. [%]	Product	Yield [%]
1[a]		>99		>99
2		90		76
3	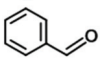	>99	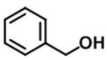	93
4	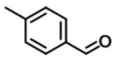	>99	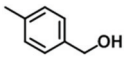	85
5	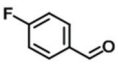	78	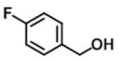	66
6	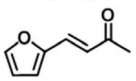	99	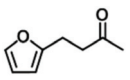	64
			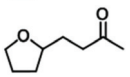	29
			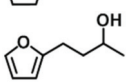	3
7	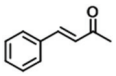	>99	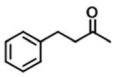	92
			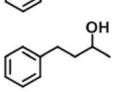	5

Reaction conditions: 3% Pd/iron silicate (10 mg), substrate (5 mmol), no solvent, H_2 (20 bar), 120 °C, 3 h. [a] Reaction was performed at 30 °C.

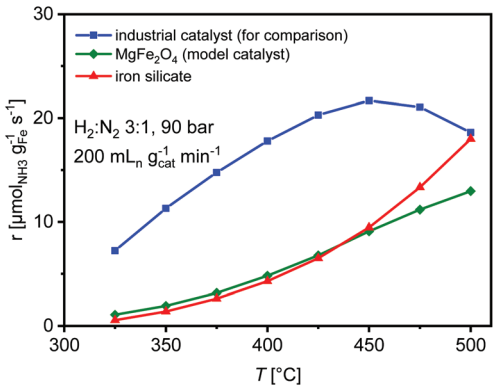

Fig. 8 Catalytic activity of the iron silicate in ammonia synthesis in comparison with an industrial catalyst and a model catalyst.

Fig. 8. The iron silicate shows indeed activity for ammonia synthesis with very similar activities as the model catalyst in the kinetic regime between 325 and 425 °C. STEM analysis of the iron silicate (Fig. S41†) shows the expected decomposition of the structure, resulting in a mixture of elemental Fe and SiO_2. Accordingly, the BET surface area decreased to *ca.* 76 $m^2\ g^{-1}$. It is noteworthy that the resulting iron shows a distinct activity already with SiO_2 as the only additional component.

Conclusion

In summary, Ferripyrophyllite, an iron silicate with a Fe–Si-ratio of 1 : 2 and 2D nanosheet morphology, was prepared from Fe powder and various silica sources under surprisingly mild conditions. While iron silicates are generally available only from natural sources or hydrothermal synthesis under extreme conditions, the developed protocol uses aqueous solutions at 100 °C in standard autoclaves or even in simple glass flasks. In-depth analytical characterizations are most consistent with a dioctahedral TOT sheet silicate of the serpentine subgroup with $Fe_2[Si_4O_{10}](OH)_2$ entities as represented schematically in Fig. 2. The obtained ferripyrophyllite has relatively high surface area and shows very high thermostability. Preliminary catalytic tests for hydrogenation of organic substrates with supported palladium nanoparticles and ammonia synthesis with the pristine material showed promising results. The straightforward preparation protocol provides flexible access to synthetic materials of this class of compounds, making them available for systematic evaluation of their properties and potential applications.

Experimental section

Material synthesis

(a) Synthesis of iron silicates (please see ESI for further experimental details and Fig. S1–S11 for iron silicate characterization by TEM and EDX analysis)†. The synthesis was performed in a 28 mL autoclave (material No. 2.4819). SBA-15 (100 mg), Fe powder (64.5 mg, $n_{Fe} : n_{Si} = 1 : 1.4$) and deionized water (5.0 mL) were mixed inside the autoclave (equipped with a glass inlet). The autoclave was tightened under air atmosphere and then heated. The starting point of the reaction time was defined for the moment at which the inner temperature of the autoclave reached 100 °C. After continuous stirring (400–450 rpm) for 24 h the autoclave was cooled down to room temperature in a controlled manner using an ice water bath. Excess Fe powder was separated without further treatment because it adsorbs on the surface of the magnetic stirring bar. The solid material was separated by centrifugation (6 K, 20 min), then washed with a mixture of H_2O and acetone ((5 + 5) mL × 2) and acetone (10 mL × 1) which were also separated by centrifugation (6 K, 20 min). Beige colored powders were obtained after drying at room temperature in the air for several minutes. The obtained powder was further purified from amorphous silica and unconverted SBA-15 *via* double treatment with an ammonia solution (6 M, 10 mL ammonia solution for 100 mg powder) at 40 °C for 16 h followed by centrifugation, washing and drying. The degree of purity is estimated to be around 90–95% judged by at least 100 TEM images.

(b) Scale-up production of iron silicate. We have scaled up the synthesis of the iron silicate using a 500 mL autoclave with 6 g SBA-15, 3.84 g iron powder and 300 mL water reacting at 100 °C. TEM and SEM-EDX mapping (Fig. S3 and S4†) show nearly the same morphology and composition. However, a higher content of SiO_2 impurity was obtained compared with the batches on a smaller scale. After reaction at 100 °C for 24 h, the powder was separated by centrifugation and further purified by double treatment of 6 M ammonia solution at 40 °C for 16 h followed by centrifugation, washing and drying.

(c) Production of iron silicates with other silica sources. Production of iron silicates with other silica sources were done similarly. Other silica sources than SBA-15 can be used for the formation of iron silicates. For example, MCM-41 can smoothly be converted under the same reaction conditions (Fig. S5 and S6†). Similar morphology can be obtained when Al (6 wt%) incorporated SBA-15 was used as silica source. One can clearly see that all four elements are very well distributed (Fig. S7 and S8†). Nanosheets could also be achieved when aerosil was used, but with lots of unreacted SiO_2 (Fig. S9†). Due to the mild reaction conditions, even production in simple glass flasks is possible.

(d) Preparation of 3 wt% Pd/iron silicate. Preparation of 3 wt% Pd/iron silicate using Chemical Fluid Deposition method was similar as preparation of 3 wt% Pd/SBA-15,[58] except the support material was iron silicate instead of SBA-15.

Catalytic reactions

(a) Hydrogenation of organic compounds. Hydrogenations were performed in a 28 mL autoclave made of hastelloy (material number: 2.4819). Under argon flushing, a glass inlet with the weighted catalyst (10 mg) and the organic substrate (5.0 mmol) was placed inside the autoclave. After tightening, the autoclave was pressurized with 20 bar H_2 at room tempera-

ture. The starting point of the reaction time was defined for the moment at which the inner temperature of the autoclave reached 120 °C (about 15 min). After 3 hours reaction time, the autoclave was cooled down to room temperature in a controlled manner using an ice water bath. The product mixture was diluted with acetone, then filtrated over RC 4 syringe filter and further analyzed *via* GC analysis.

(b) Ammonia synthesis. The ammonia synthesis tests were performed in a commercial flow set-up equipped a plug flow reactor as a synthesis reactor as well as an online IR-detector (Emerson X-stream) for quantitative gas analysis of NH_3 and H_2O. 0.838 g of the catalyst precursor (grain fraction of 250–425 μm) was diluted with ~1 g SiC (average grain size 154 μm). Beyond and below the catalyst bed, a bed of pure SiC was placed, held in position by a glass wool plug at the entrance and exhaust of the reactor. The sample was reduced by heating it in a gas flow of 440 mL_n min^{-1} (75% H_2, 25% N_2) with a heating rate of 1 K min^{-1} up to 500 °C. Afterwards, the conditions were kept constant for around 88 h. The pressure was not elevated. The resulting pressure in the reactor (due to pressure drop) was in the range of 3–4 bar. For high pressure activity measurements, the temperature was kept at 500 °C, and the pressure was increased up to 90 bar. During the pressure increasing, the total flow was also increased to accelerate this procedure. After 90 bar was reached, the total flow was adjusted to 200 mL_n min^{-1} (75% H_2, 25% N_2). The temperature was kept constant for 48 h, and afterwards, temperature steps at 475, 450, 425, 400, 375, 350, 325, 350, 375, 400, 425, 450, 475 and 500 °C were adjusted. Heating rates between the temperature steps were set to be 1 K min^{-1}. All temperatures of the temperature steps were kept constant for 155 min

Materials characterization (please see ESI for further details on the characterization methods†). Obtained composite materials were characterized by elemental analysis, transmission electron microscopy (TEM), energy-dispersive X-ray spectroscopy (EDX) and scanning transmission electron microscopy (STEM), Mössbauer spectroscopy, electron paramagnetic resonance (EPR), pair distribution function (PDF) analysis, Fourier-transform infrared spectroscopy (FTIR), *in situ* diffuse reflectance infrared fourier spectroscopy (DRIFT), SQUID measurement, thermogravimetric analysis–mass spectrometry (TG–MS), sorption isotherms (N_2-BET), X-ray diffraction (XRD) and X-ray photoelectron spectroscopy (XPS).

Authors contribution

Y.X. Qiao performed the material synthesis and the catalytic hydrogenation experiments of the organics. B. Spliethoff discovered the formation of this nanosheet material through TEM imaging and analyzed it by this method in combination with EDX. N. Theyssen and W. Leitner both supervised the project. F. Schüth gave insightful guidance as well. C. Weidenthaler performed X-ray diffraction (XRD), X-ray photoelectron spectroscopy (XPS) and pair distribution function (PDF) analysis. W. Schmidt performed TG-DSC-MS measurement. G. Prieto performed NH_3-TPD measurement, and C. Ochoa-Hernández made Pyridine-FTIR and DRIFT analysis. E. Bill and S.F. Ye analyzed the material with Mössbauer and electron paramagnetic resonance (EPR) spectroscopy. They determined the magnetic properties as well. J. Folke and H. Ruland performed the catalytic ammonia synthesis. Y.X. Qiao wrote the initial manuscript with input from all authors and N. Theyssen and W. Leitner modified the paper in its present form. All authors discussed the results and edited the manuscript before submission.

Conflicts of interest

There are no conflicts to declare.

Acknowledgements

The authors gratefully acknowledge the following people for support with analytical measurements and data analysis: Hans-Josef Bongard (SEM-EDX), Silvia Palm (EDX bulk), Adrian Schlüter (TEM), Norbert Pfänder (STEM), Jan Ternieden and Jan Nicolas Büscher (XRD and XPS), Prof. Dr Osamu Terasaki and Dr Yanghang Ma (3D electron diffraction tomography: failed due to the poor crystallinity and stability under strong beam irradiation), Dr Nicolas Duyckaerts (NH_3-TPD measurements), Kai Jeske (GC gas analysis), Dr Yuxiao Ding (ATR-IR) and Dr Zhengwen Cao (titration). The authors also would like to thank Prof. Dr Robert Schlögl, Dr Thomas Lunkenbein, Fabian Pienkoß and Dr Gaetano Calvaruso for helpful and enthusiastic discussions, as well as Niklas Fuhrmann and Lars Winkel for technical support. The studies were carried out as part of our activities in the Cluster of Excellence "Tailor-Made Fuels from Biomass" (EXC 236) and "The Fuel Science Center" funded by the Deutsche Forschungsgemeinschaft (DFG, German Research Foundation) under Germany's Excellence Strategy – Exzellenzcluster 2186 "The Fuel Science Center" ID: 390919832. Open Access funding provided by the Max Planck Society.

References

1 F. Liebau, *Structural Chemistry of Silicates: Structure, Bonding, and Classification*, Springer, 1st edn, 1985.
2 M. F. Brigatti, E. Galán and B. K. G. Theng, in *Handbook of Clay Science*, ed. F. Bergaya and G. Lagaly, Elsevier, Oxford, 2013, 5, pp. 21–81.
3 Z. F. Bian and S. Kawi, *Catal. Today*, 2020, **339**, 3–23.
4 B. W. Evans and S. J. Guggenheim, *Rev. Mineral. Geochem.*, 1988, **19**, 225–294.
5 M. Claverie, A. Dumas, C. Carême, M. Poirier, C. Le Roux, P. Micoud, F. Martin and C. Aymonier, *Chem. – Eur. J.*, 2018, **24**, 519–542.

6 F. V. Chukhrov, B. B. Zvyagin, V. A. Drits, A. I. Gorshkov, L. P. Ermilova, E. A. Goilo and E. S. Rudnitskaya, in *Developments in Sedimentology*, ed. M. M. Mortland, V. C. Farmer, Elsevier, Oxford, 1979, 27, 55–64.
7 F. V. Chukhrov, B. B. Zvyagin, V. A. Drits, A. I. Gorshkov, L. P. Ermilova, E. A. Goilo and E. S. Rudnitskaya, Izvestiya Akademii Nauk SSSR, *Ser. Geol.*, 1979, **2**, 5–20.
8 J. M. D. Coey, F. V. Chukhrov and B. B. Zvyagin, *Clays Clay Miner.*, 1984, **32**, 198–204.
9 M. F. Brigatti and E. Galan, In *Handbook of Clay Science*, ed. F. Bergaya, B. K. G. Theng and G. Lagaly, Elsevier, Oxford, 2006, 1, p. 19–86.
10 D. Zhang, C.-H. Zhou, C.-X. Lin, D.-S. Tong and W.-H. Yu, *Appl. Clay Sci.*, 2010, **50**, 1–11.
11 A. Loaiza-Gil, J. Arenas, M. Villarroel, F. Imbert, H. del Castillo and B. Fontal, *J. Mol. Catal. A: Chem.*, 2005, **228**, 339–344.
12 M. V. Sivaiah, S. Petit, M. F. Beaufort, D. Eyidi, J. Barrault, C. Batiot-Dupeyrat and S. Valange, *Microporous Mesoporous Mater.*, 2011, **140**, 69–80.
13 C. Qiu, J. Jiang and L. H. Ai, *ACS Appl. Mater. Interfaces*, 2016, **8**, 945–951.
14 H. R. Yue, Y. J. Zhao, S. Zhao, B. Wang, X. B. Ma and J. L. Gong, *Nat. Commun.*, 2013, **4**, 2339, DOI: 10.1038/ncomms3339.
15 J. Myers and H. P. Eugster, *Contrib. Mineral. Petrol.*, 1983, **82**(1), 75–90.
16 D. H. Lindsley, B. T. C. Davis and I. D. Macgregor, *Science*, 1964, **144**, 73–74.
17 S. Sueno, M. Cameron and C. T. Prewitt, *Am. Mineral.*, 1976, **61**, 38–53.
18 D. Zherebetskyy, G. Amthauer and M. Grodzicki, *Phys. Chem. Miner.*, 2010, **37**, 455–464.
19 J. Smuts, J. G. D. Steyn and J. C. A. Boeyens, *Acta Crystallogr.*, 1969, **B25**, 1251–1255.
20 P. A. Van Aken, G. Miehe, A. B. Woodland and R. J. Angel, *Eur. J. Mineral.*, 2005, **17**, 723–731.
21 F. W. Clarke, *Monogr. U.S. Geol. Surv.*, 1903, **43**, 243–247.
22 L. G. Kwasha, *Meteoritika*, 1976, **35**, 136–138.
23 S. J. Datta, C. Khumnoon, Z. H. Lee, W. K. Moon, S. Docao, T. H. Nguyen, I. C. Hwang, D. Moon, P. Oleynikov, O. Terasaki and K. B. Yoon, *Science*, 2015, **350**, 302–306.
24 Y. Y. Wu, Z. H. Fu, D. L. Yin, Q. Xu, F. L. Liu, C. L. Lu and L. Q. Mao, *Green Chem.*, 2010, **12**, 696–700.
25 J. J. Wang, W. J. Xu, J. W. Ren, X. H. Liu, G. Z. Lu and Y. Q. Wang, *Green Chem.*, 2011, **13**, 2678–2681.
26 A. R. González-Elipe, J. P. Espinós, G. Munuera, J. Sanz and J. M. Serratosa, *J. Phys. Chem.*, 1988, **92**, 3471–3476.
27 A. Sharma, H. Jain and A. C. Miller, *Surf. Interface Anal.*, 2001, **31**, 369–374.
28 A. Mekki, D. Holland, C. F. McConville and M. Salim, *J. Non-Cryst. Solids*, 1996, **208**, 267–276.
29 T. Yamashita and P. Hayes, *Appl. Surf. Sci.*, 2008, **254**, 2441–2449.
30 K. Hirao, N. Soga and M. Kunugi, *J. Am. Ceram. Soc.*, 1979, **62**, 109–110.
31 M. M. Nasrallah, S. K. Arif and A. M. Bishay, *Mater. Res. Bull.*, 1984, **19**, 269–277.
32 M. G. Ferreira da Silva and C. Bender Koch, *J. Sol-Gel Sci. Technol.*, 1997, **8**, 311–314.
33 K. Bachari, A. Touileb and M. Lamouchi, *Transition Met. Chem.*, 2009, **34**, 529–537.
34 C. S. Ray, S. T. Reis, W. M. Pontuschka, J. B. Yang, F. F. Sene, J. M. Giehl, C. W. Kim and S. Sen, *J. Non-Cryst. Solids*, 2006, **352**, 3677–3684.
35 L. Bonneviot and D. Olivier, *Ferromagnetic Resonance, Catalyst Characterization*, Springer, Boston, 1994, 7, p181–p214.
36 T. Proffen, S. J. L. Billinge, T. Egami and D. Louca, *Z. Kristallogr.*, 2003, **218**, 132–143.
37 T. Proffen, K. L. Page, S. E. McLain, B. Clausen, T. W. Darling, J. A. TenCate, S.-Y. Lee and E. Ustundag, *Z. Kristallogr.*, 2005, **220**, 1002–1008.
38 I. E. Wachs, *Catal. Today*, 1996, **27**, 437–455.
39 N. Maxim, A. Overweg, P. J. Kooyman, J. H. M. C. van Wolput, R. W. J. M. Hanssen, R. A. van Santen and H. C. L. Abbenhuis, *J. Phys. Chem. B*, 2002, **106**, 2203–2209.
40 C. L. Wang and L. L. Shaw, *J. Sol-Gel Sci. Technol.*, 2014, **72**, 602–614.
41 M. D. Yuniati, T. Hirajima, H. Miki and K. Sasaki, *Mater. Trans.*, 2015, **56**, 1733–1741.
42 Y. K. Sun, X. Bai, T. Li, G. X. Lu, Y. X. Qi, N. Lun, Y. Tian and Y. J. Bai, *J. Alloys Compd.*, 2016, **686**, 318–325.
43 S. Vahur, A. Teearu, P. Peets, L. Joosu and I. Leito, *Anal. Bioanal. Chem.*, 2016, **408**, 3373–3379.
44 J. Petrovič, L. Ševula and M. Pisárčik, *Chem. Pap.*, 1985, **39**, 59–68.
45 S. Musić, I. Czakó-Nagy, S. Popović, A. Vértes and M. Tonković, *Croat. Chem. Acta*, 1986, **59**, 833–851.
46 H. Aliyan, R. Fazaeli and R. Jalilian, *Appl. Surf. Sci.*, 2013, **276**, 147–153.
47 M. S. Kumar, J. Pérez-Ramírez, M. N. Debbagh, B. Smarsly, U. Bentrup and A. Brückner, *Appl. Catal., B*, 2006, **62**, 244–254.
48 M. Schwidder, M. S. Kumar, U. Bentrup, J. Pérez-Ramírez, A. Brückner and W. Grünert, *Microporous Mesoporous Mater.*, 2008, **111**, 124–133.
49 E. Paterson, R. Swaffield and D. R. Clark, *Thermochim. Acta*, 1982, **54**, 201–211.
50 S. Musić, S. Krehula and S. Popović, *Mater. Lett.*, 2004, **58**, 444–448.
51 X. W. Song and J.-F. Boily, *J. Phys. Chem. A*, 2016, **120**, 6249–6257.
52 Q. Y. Hu, D. Y. Kim, W. G. Yang, L. X. Yang, Y. Meng, L. Zhang and H.-K. Mao, *Nature*, 2016, **534**, 241–244.
53 C. L. Tan, X. H. Cao, X. J. Wu, Q. Y. He, J. Yang, X. Zhang, J. Z. Chen, W. Zhao, S. K. Han, G.-H. Nam, M. Sindoro and H. Zhang, *Chem. Rev.*, 2017, **117**, 6225–6331.
54 D. H. Deng, K. S. Novoselov, Q. Fu, N. F. Zheng, Z. Q. Tian and X. H. Bao, *Nat. Nanotechnol.*, 2016, **11**, 218–230.
55 X. W. Wang, G. Z. Sun, N. Li and P. Chen, *Chem. Soc. Rev.*, 2016, **45**, 2239–2262.

56 Y. L. Xi, J. C. Zhuang, W. C. Hao and Y. Du, *ChemElectroChem*, 2019, **6**, 2841–2851.
57 C. N. R. Rao, K. Gopalakrishnan and U. Maitra, *ACS Appl. Mater. Interfaces*, 2015, **7**, 7809–7832.
58 Y. X. Qiao, N. Said, M. Rauser, K. Yan, F. Qin, N. Theyssen and W. Leitner, *Green Chem.*, 2017, **19**, 977–986.
59 M. Armbrüster, M. Behrens, F. Cinquini, K. Föttinger, Y. R. Grin, A. Haghofer, B. Klötzer, A. Knop–Gericke, H. Lorenz, A. Ota, S. Penner, J. Prinz, C. Rameshan, Z. Révay, D. Rosenthal, G. Rupprechter, P. Sautet, R. Schlögl, L. D. Shao, L. Szentmiklósi, D. Teschner, D. Torres, R. Wagner, R. Widmer and G. Wowsnick, *ChemCatChem*, 2012, **4**, 1048–1063.
60 W. Ludwig, A. Savara, K.-H. Dostert and S. Schauermann, *J. Catal.*, 2011, **284**, 148–156.
61 K. F. Ortega, D. Rein, C. Lüttmann, J. Heese, F. Özcan, M. Heidelmann, J. Folke, K. Kähler, R. Schlögl and M. Behrens, *ChemCatChem*, 2017, **9**, 659–671.
62 R. Schlögl, *Angew. Chem., Int. Ed.*, 2003, **42**, 2004–2008.
63 A. Hellman, E. J. Baerends, M. Biczysko, T. Bligaard, C. H. Christensen, D. C. Clary, S. Dahl, R. van Harrevelt, K. Honkala, H. Jonsson, G. J. Kroes, M. Luppi, U. Manthe, J. K. Nørskov, R. A. Olsen, J. Rossmeisl, E. Skúlason, C. S. Tautermann, A. J. C. Varandas and J. K. Vincent, *J. Phys. Chem. B*, 2006, **110**, 17719–17735.
64 Y. Tanabe and Y. Nishibayashi, *Coord. Chem. Rev.*, 2013, **257**, 2551–2564.
65 H. Tanaka, Y. Nishibayashi and K. Yoshizawa, *Acc. Chem. Res.*, 2016, **49**, 987–995.
66 M. Hölscher and W. Leitner, *Chem. – Eur. J.*, 2017, **23**, 11992–12003.